NANO LETTERS
Letter
Cite This: Nano Lett. 2018, 18, 4100−4106
pubs.acs.org/NanoLett

Damage Accumulation in Silica Glass Nanofibers

Silvia Bonfanti,[†,§] Ezequiel E. Ferrero,[*,†,‡,§] Alessandro L. Sellerio,[†] Roberto Guerra,[†] and Stefano Zapperi[*,†,¶]

[†]Center for Complexity and Biosystems, Department of Physics, University of Milano, via Celoria 16, 20133 Milano, Italy
[‡]CONICET, Centro Atómico Bariloche, Av. Bustillo 9500, 8400 S. C. de Bariloche, Río Negro Argentina
[¶]Consiglio Nazionale delle Ricerche, Istituto di Chimica della Materia Condensata e di Tecnologie per l'Energia, Via R. Cozzi 53, 20125 Milano, Italy

Supporting Information

ABSTRACT: The origin of the brittle-to-ductile transition, experimentally observed in amorphous silica nanofibers as the sample size is reduced, is still debated. Here we investigate the issue by extensive molecular dynamics simulations at low and room temperatures for a broad range of sample sizes, with open and periodic boundary conditions. Our results show that small sample-size enhanced ductility is primarily due to diffuse damage accumulation, that for larger samples leads to brittle catastrophic failure. Surface effects such as boundary fluidization contribute to ductility at room temperature by promoting necking, but are not the main driver of the transition. Our results suggest that the experimentally observed size-induced ductility of silica nanofibers is a manifestation of finite-size criticality, as expected in general for quasi-brittle disordered networks.

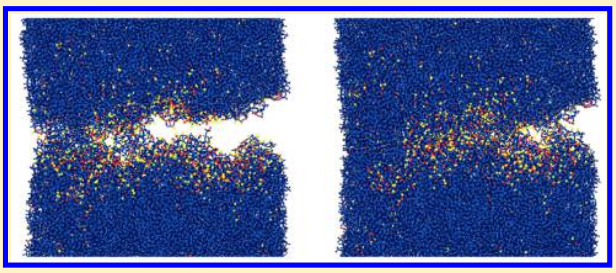

KEYWORDS: *Silica, nanowires, nanofibers, fracture, ductility*

Despite its relevance for several applications, from basic tools to nanotechnology, the understanding of the mechanical response of amorphous materials is still incomplete. The long-standing engineering issue is to ensure simultaneously high strength and extended deformability. These two properties are unfortunately nearly mutually exclusive: very strong structural materials (e.g., ceramics) can sustain enormous stresses but fail catastrophically, with no signs of plasticity, while metallic alloys are able to sustain a degree of plastic strain by sacrificing strength. We broadly distinguish two ideally opposite kinds of mechanical failure: brittle failure where a catastrophic fracture event happens soon after the elastic deformation limit, and ductile failure involving a considerable amount of plastic deformation before failure. Between these two extremes lies the quasi-brittle behavior, observed in many disordered materials such as concrete and rocks, where failure is preceded by extensive damage accumulation.[1]

Traditionally, a transition from brittle to ductile failure in the same material can be achieved by decreasing the strain rate[2,3] or increasing the temperature,[2,4,5] but it is also possible to reach the same goal by modifying sample preparation and composition. For example, silica glasses quenched under increasingly high pressures show an enhanced ductility,[6] suggesting a role for increased defect concentration. Recent results are changing the conventional view of the brittle-to-ductile transition (BDT) suggesting that it is possible to induce ductility just by reducing the sample size toward the nanoscale,[7−12] as demonstrated for silica glass nanofibers under tensile load.[9,10]

The physical origin of this sample-size-induced BDT in silica glasses is currently debated. The main physical mechanism invoked to explain the onset of ductility at the nanoscale involves the interplay between surface and bulk effects, whose relative importance clearly changes with the sample size. This appears to be a widely observed phenomenon, manifested not only in amorphous solids[13−16] but also, to some extent, in crystals.[14,17,18] A "fluid-like" surface layer similar to those observed in glassy polymers[19,20] was reported in recent experiments on amorphous silica.[9,10] The idea is that when stress is applied, surface atoms (and groups of atoms), more mobile than in the bulk due to lower bond coordination, would be the first to switch bonds and rearrange or even migrate along the surface. As the fiber diameter decreases, this surface effect is expected to have a growing influence in the deformation process with respect to bulk processes like crack nucleation and propagation.

To shed light on the mechanism leading to the observed BDT in silica glass, we perform extensive molecular dynamics simulations. The advantages of this approach are the direct visualization of microscopic bond breaking and the possibility to compare open and periodic boundary conditions to highlight the role of the free surface. Our results demonstrate that bond breaking plays a central role for the enhanced small-size

Received: February 2, 2018
Revised: May 8, 2018
Published: June 1, 2018

DOI: 10.1021/acs.nanolett.8b00469
Nano Lett. 2018, 18, 4100−4106

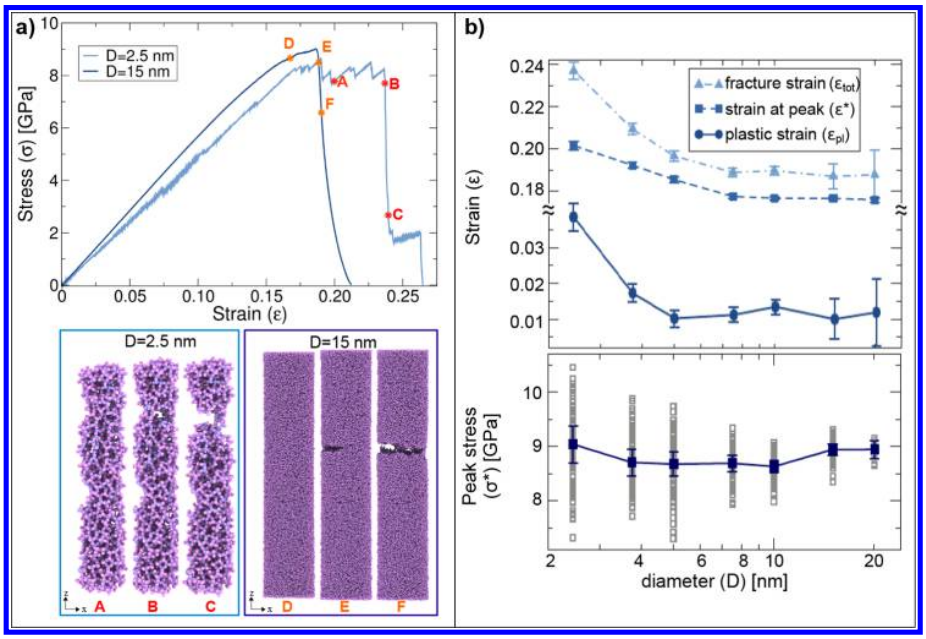

Figure 1. Brittle-to-ductile crossover as the sample size is reduced. (a) (top) Stress−strain curves of two typical samples of diameter D = 2.5 nm and D = 15 nm and (bottom) snapshots of the same nanofibers during the deformation at configurations marked by labels on the corresponding stress curves (violet spheres = Si atoms, pink spheres = O atoms; arbitrary scale). See Movies S3 and S4 for full animations. (b) (top) Deformation up to peak stress, $\epsilon^* \equiv \epsilon(\sigma_{max})$, total deformation, ϵ_{tot}, before fracture, plastic deformation, $\epsilon_{pl} \equiv (\epsilon_{tot} - \epsilon^*)$, and (bottom) the average maximum stress σ^* as a function of the sample diameter. In the latter, scattered symbols show the σ^* value of each individual sample, while blue squares correspond to the average.

ductility, while free surfaces only play a role at high temperatures.

Results. *Low Temperature Deformation of Amorphous Silica Glass Nanowires.* We simulate the tensile deformation of cylindric nanofibers of amorphous silica glass (a-SiO_2) using different sample sizes with open boundary conditions (obc). To disentangle the role of structural disorder from thermal fluctuations, we first perform simulations at very low temperature, ∼ 1 K (see Methods section for details).

Figure 1a shows typical stress−strain curves obtained from the deformation of two cylindric nanofibers of different sizes, together with visual snapshots at different applied strains during the deformation at 1 K. For large fiber diameters, we observe an abrupt fracture right after the deviation from a purely elastic regime, signaling a brittle response also reflected by the relatively sharp crack surfaces formed in the fracture region. At very small diameters, beyond the elastic limit, we observe instead a sustained stress−strain curve of a jagged shape and a more irregular crack surface with appreciable necking at the onset of fracture. We note that, differently than in metallic glass nanofibers[11] where the crack is oriented at 45° with respect to the loading direction, in SiO_2 glasses,[9] the crack is oriented at 90°. This is due to the fact that metallic glasses fail along the direction of maximum shear, while silica glasses fail along the direction of maximum tensile stress.

To quantify the brittle-to-ductile crossover, we average over several stress−strain curves four characteristic quantities: (i) the strain at which the engineering stress peaks, ϵ^*. This would be ideally a measure of elastic elongation previous to the yielding point, but since a non-negligible, and sometimes important, plastic deformation occurs before the stress peak, this does not necessarily coincide with the plastic onset; (ii) the total strain before fracture, ϵ_{tot}; (iii) the plastic strain, $\epsilon_{pl} \equiv (\epsilon_{tot} - \epsilon^*)$; (iv) the maximum stress or peak stress, σ^*. Figure 1b (top panel) shows that ϵ^*, converging to ∼17.5% at large diameters, starts to increase below a threshold diameter of ∼8 nm and exceeds ∼20% at the smallest considered size. Such increased endurable strain in the preyield deformation stage is in good agreement with experimental data.[10] Similarly, the sample averaged ϵ_{tot} increases below the same threshold diameter from ∼19% up to ∼24%, more steeply than ϵ^*, which reflects on the plastic strain ϵ_{pl} trend.

Turning our attention to the fracture strength, the peak stress value σ^* shown in Figure 1b (bottom panel) presents a distribution of values broader for smaller samples, without an appreciable variation of the average with the system size, at least for the range of sizes we study. The experimental evidence of Luo et al.[9] showing a weak strength increase at decreasing D could be related to the broadening of the sample-to-sample fluctuations that we observe. Furthermore, our data clearly support a nanoscale size effect, which reduces the elastic modulus, E, at a small size, suggesting a weaker contribution from the surface region (see Supporting Information, Figure S1).

Origin of Small-Size Ductility. We inspect the x-y mean-squared displacement of the atoms composing the smallest nanofiber at different radial positions (see Supporting Information, Figures S2 and S3). Notice that, in our simulations, regardless of the sample diameter, the outer layer, defined as the layer in which the density drops from its bulk value to zero, has an approximate fixed width of 0.5 nm (see Supporting Information, Figure S4). Therefore, as we decrease the sample diameter, the surface layer becomes more and more relevant. We find indeed that even at very low temperatures, atoms in the outer rim display a much larger mobility than the others. In particular, we estimate a diffusion

DOI: 10.1021/acs.nanolett.8b00469
Nano Lett. 2018, 18, 4100−4106

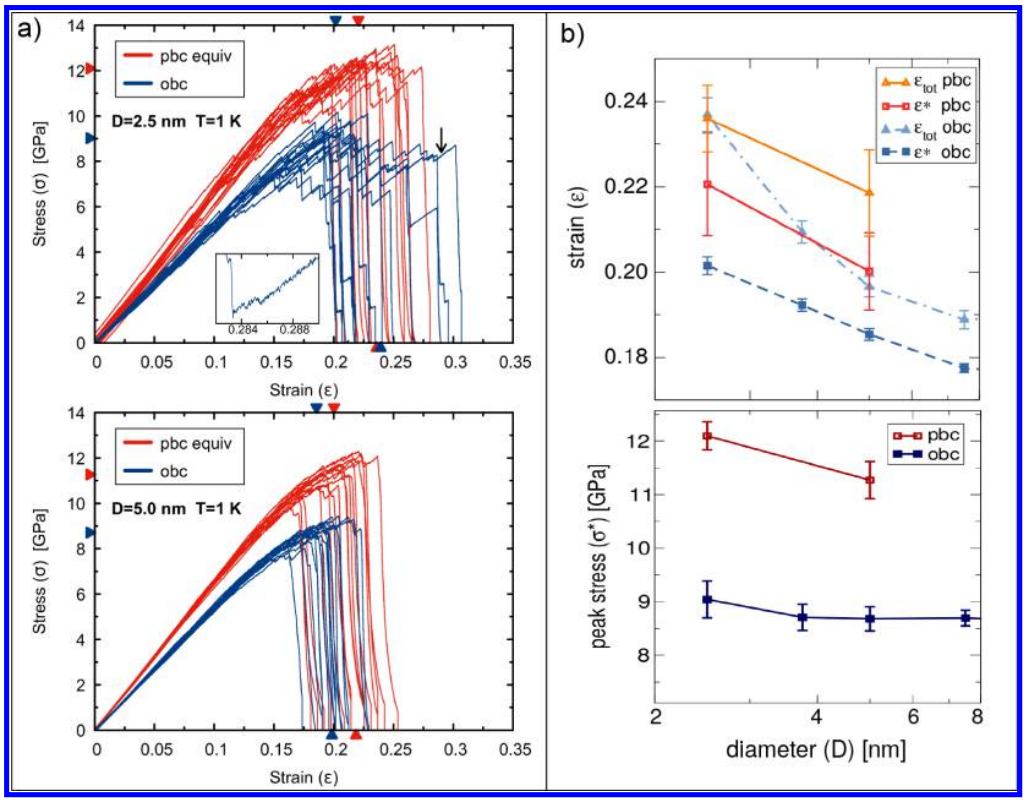

Figure 2. Obc and pbc comparison for small sample sizes at 1 K. (a) Stress−strain curves of obc and pbc samples with D = 2.5 nm (top panel) and D = 5 nm (bottom panel) at T = 1 K. Triangles at left, top, and bottom axes report σ^*, ϵ^*, and ϵ_{tot}, respectively, averaged over 100 runs (16 shown). The inset in the top panel is a magnification of the region pointed by the arrow. (b) Average values comparison as a function of size: (top panel) strain at peak ϵ^*, and rupture strain ϵ_{tot}, and (bottom panel) peak stress σ^*.

coefficient at the surface that is from 4 to 5 times larger than in the bulk. This result is in agreement with the role of surface-induced plasticity advocated in Wingert et al.[10] To corroborate this point, we analyze the behavior of the equivalent small system size samples but with periodic boundary conditions (pbc). We perform simulations of the tensile deformation of samples of length, L, and cross-section, $M \times M \equiv \pi D^2/4$, with applied pbc along the x and y directions (see Methods).

Figure 2a shows a comparison of the stress−strain curves for the D = 2.5 nm and D = 5.0 nm samples at T = 1 K for pbc and obc. Size-dependent averages of ϵ_{tot}, ϵ^*, and σ^* are reported in Figure 2b. Our findings show that pbc samples present larger stress peaks, while preserving similar or even larger attainable strains ϵ_{tot}. Furthermore, the smallest sample clearly displays a large plastic-like deformation regime, even when no surface is present (pbc), suggesting that ductility can not be due only to surface effects.

To investigate the origin of the observed ductile-like behavior, we inspect the evolution of the atomic coordination during deformation, a method previously used in numerical simulations of amorphous silica, both in quiescent relaxation[21,22] and tensile deformation,[15,16] to reveal bond switching, an important source of stress release.[13,14] A careful inspection shows that both small (Figure 3a) and large (Figure 3b) obc systems display similar trends in the variation of the atomic coordination. The same is observed for pbc systems. After an initial stationary period with no changes in the coordination number, roughly coincident with the purely elastic phase of the deformation, we observe a progressive decrease of well-coordinated Si^{4+} and O^{2-} atoms, compensated by an increase of under-coordinated silicon (Si^{3+}, Si^{2+}; magenta curve in the figure) and oxygen (O^{1-}) atoms (see also Supporting Information, Figure S5). A similar mechanism is evinced from the change of the Si−O−Si angle distribution during the tensile deformation, showing a main peak at ∼141.5°, which reduces linearly at an increasing applied strain, in favor of accumulation at larger angles, especially around ∼161° (see Supporting Information, Figure S6).

These results provide clear evidence that damage accumulation is taking place. While these localized events might go unnoticed in the stress-strain curve of a large system, in small systems, they correspond to relatively large stress drops (correlated with energy jumps, see Supporting Information, Figure S5). We therefore conclude that the released stress due to bond breaking is at the origin of the ductility shown by our small-sized samples.

Note that some damage is already present in the unstretched samples in terms of intrinsic defects. In this respect, more defective samples are consistently shown to break earlier, being less capable of accumulating damage (see Supporting Information, Figure S7). A more refined structure−property relationship could be provided by the identification of polyhedral clusters in the SiO_2 glass, some of which have been identified as energetically favored and thus more stable.[23] The failure statistics could therefore be described, in a coarse-grained like fashion, in terms of the interaction among these hard clusters.

DOI: 10.1021/acs.nanolett.8b00469
Nano Lett. 2018, 18, 4100−4106

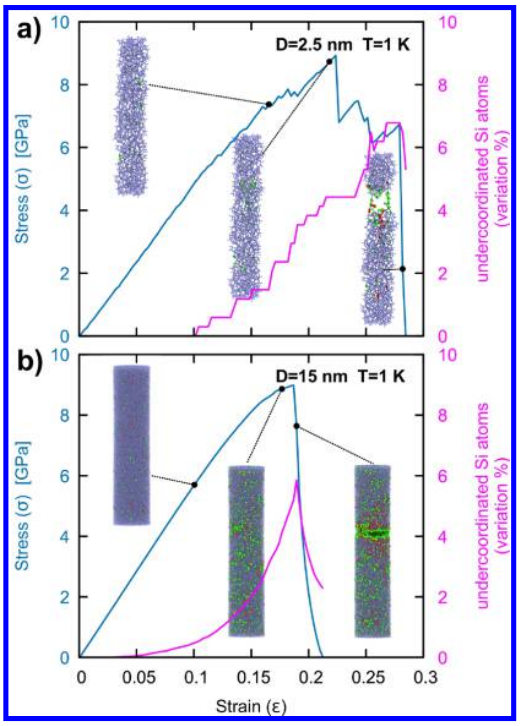

Figure 3. Coordination and damage accumulation in obc samples at 1 K. Stress (blue) and percent variation of the number of undercoordinated Si atoms (magenta) as a function of the applied strain for cylindric nanofibers with (a) D = 2.5 nm and (b) D = 15 nm. Snapshots reported in green and red are the dynamically broken and newly formed (or reformed) bonds, respectively (see Movies S3 and S4 for full animations).

Stress-Drop Statistics Display Power Laws. In order to further characterize the observed ductility, we study the statistical features of stress drops during loading. For each set of samples of a given size, we analyze the stress-time series (such as those reported in Figure 2a). After the initial elastic regime, we locate stress drops $\Delta\sigma$ following a standard procedure:[24−26] we identify time intervals where the negative time derivative of the stress, $d\sigma/dt$, exceeds a threshold and compute the corresponding stress drops (see the lower inset of Figure 4a for a visual explanation).

Figure 4 shows stress-drop distributions for different system sizes, temperatures, and boundary conditions. In the obc case, we observe a size-dependent crossover from an exponential distribution at a "small" $\Delta\sigma$ to a power-law distribution at a "large" $\Delta\sigma$ (Figure 4a). The exponentially distributed small drops (e.g., $\Delta\sigma < 3 \times 10^{-2}$GPa for the D = 2.5 nm case) are associated with a surface effect, since they are not present in pbc simulations (see Figure 4b) and correspond to small and short localized rearrangements occurring during the loading phases (see the inset of Figure 2). The upper inset of Figure 4a reports a rescaled log-lin plot showing both the "thermal-like" exponential distribution of these small drops and their disappearance as the system-size increases. (The crossover to a power-law distribution moves toward smaller values of $\Delta\sigma$ as D increases.)

The observation of a power-law tail in $P(\Delta\sigma)$ for all system sizes suggests the presence of correlated events and collective behavior causing larger stress drops. Such an avalanche statistics associated with fracture can be understood via simple arguments based on percolation and mean-field theory.[27] The deformation proceeds through localized bond failures that provoke a stress redistribution in the rest of the samples that can trigger other failure events through a cascade mechanism. An explicit correlation between stress drops and change in atomic coordination (bond breaking) is reported in the Supporting Information, Figure S5. Notice that the power-law distribution $P(\Delta\sigma) \sim \Delta\sigma^{-\tau}$ appears both for obc and pbc samples at low temperature (see Figure 4b). For the system sizes and strain rate used here, it decays with the exponent found in the range $\tau \sim 1.7-2$ depending on the conditions. We have checked that the exponent does not depend significantly on the chosen threshold (see Supporting Information, Figure S8). This value is somewhat larger than the mean-field exponent τ = 3/2 expected according to Shekhawat et al.[27] In our interpretation, the disagreement is mainly due to the very large deformation rate adopted in our simulations ($\dot{\epsilon} = 2.5 \times 10^8$ s^{-1}), which is far away from the quasistatic conditions employed in Shekhawat et al.[27] Furthermore, as shown by several works devoted to the plastic deformation of amorphous solids,[28] the avalanche-related critical exponents measured in spatial models in d = 2 and d = 3 as well as in experiments often differ from mean-field theory. We also measure the distribution of waiting times, T_w, between stress drops, which decays as a

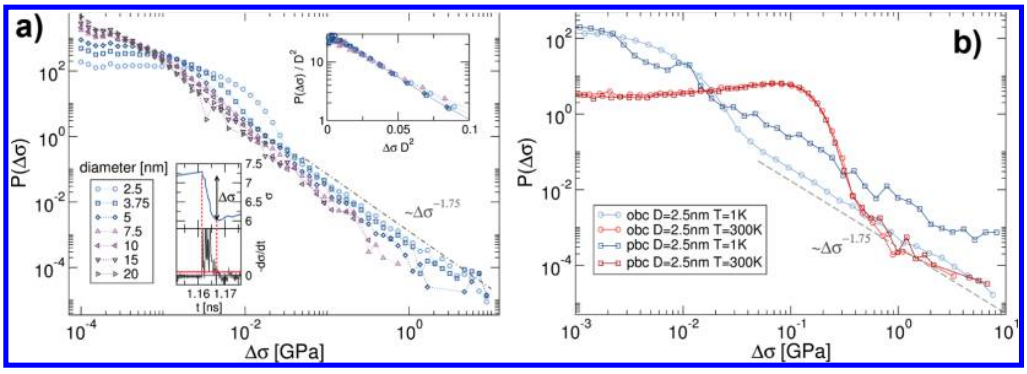

Figure 4. Stress-drop distributions. (a) $P(\Delta\sigma)$ for different sample sizes with obc. The main plot shows a power law distribution $P(\Delta\sigma) \sim \Delta\sigma^{-\tau}$ for the larger $\Delta\sigma$ with exponent $\tau \sim 1.75$; (upper inset) Lin-log plot of the $\Delta\sigma \rightarrow \Delta\sigma D^2$ scaling, showing a collapse of the distributions for small stress drops; (lower inset) example of stress drop and its derivative. Alternative thresholds are also shown. (b) Stress-drop distributions for different temperatures and boundary conditions for the smallest system size.

DOI: 10.1021/acs.nanolett.8b00469
Nano Lett. 2018, 18, 4100−4106

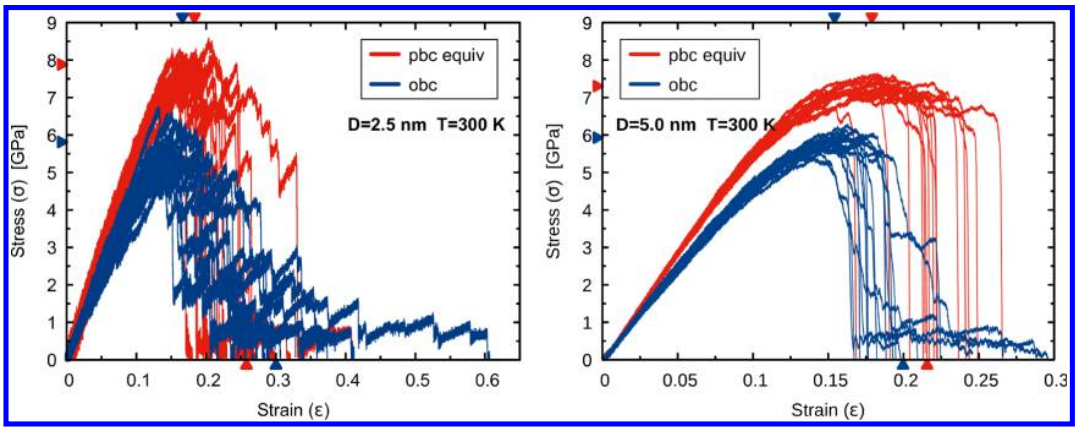

Figure 5. Stress−strain curves comparison at 300 K. Stress−strain curves of obc and pbc samples with D = 2.5 nm (left panel) and D = 5 nm (right panel) at T = 300 K. Triangles at left, top, and bottom axes report σ^*, ϵ^*, and ϵ_{tot}, respectively, averaged over 32 runs (16 shown).

power law $P(T_w) \sim T_w^{-\alpha}$, with an exponent $\alpha \simeq 1.5$ (see Supporting Information, Figure S9).

In Figure 4b, we compare the cases of $T \simeq 1$ K and $T \simeq 300$ K for both obc and pbc. At high temperatures, $P(\Delta\sigma)$ is exponential in practically all of its extension and is indistinguishable for pbc and obc cases, only recovering a power-law shape at its latest stage (and this thermal feature seems to be quite general, as has been recently observed in the displacement distribution following bond breaking of a model gel[29]), suggesting that the jerkiness of the stress-time series at high temperatures (Figure 5) is mainly thermally induced. This observation confirms our interpretation as "thermal-like" of the small stress discharges happening at $T \simeq 1$ K for the obc pillars.

Thermal Effects Increase Ductility through Necking. Finally, to clarify the role of thermally activated events, we compare obc−pbc simulations at T = 300 K (see Figure 5). When the temperature is raised in both obc and pbc, the maximum stress σ^* is reduced with respect to the low temperature case (Figure 2), owing to the reduced rigidity of the sample. On the other hand, the maximum strain, ϵ_{tot}, increases with temperatures only for obc, while no significant changes are observed for pbc, in agreement with Pedone et al.[30] The increase in strain in obc is due to re-entrant strengthening, the linear $\sigma(\epsilon)$ segments with a small positive slope, signaling the occurrence of necking. Since the Young modulus is size dependent (Figure S1), we can connect the slope of these segments to the neck thickness, showing a progressive reduction of the narrowing size until, at very low stress values, these segments become almost horizontal, meaning that a single bond is bridging the two detaching pieces of the fiber. We notice that during this process, thermal effects become more pronounced as necking starts. As a consequence, plasticity effects grow and become dominant in the last part of the process. We further note that surface effects become detrimental already at D = 5 nm by reducing the average ϵ_{tot} with respect to pbc. We expect, however, that the threshold diameter for such effect would shift toward a larger D at the slower strain rates typically employed in experiments.

Discussion. Amorphous silica glass represents the quintessential brittle material, failing abruptly in the elastic regime. Yet, recent experimental measurements revealed that nanoscale silica fibers become increasingly ductile as the size is decreased.[7−12] The origin of this puzzling size-induced brittle-to-ductile transition is still debated with possible explanations based on surface fluidization.[9,10] Indeed, experiments and simulations report evidence of a boundary layer where atoms are more mobile.[9,10] Since the ratio of surface to volume increases as the sample size is decreased, it is conceivable to assume that plastic relaxation at the surface becomes more prevalent thus explaining the observed transition.

Here, we tackled the question by molecular dynamics simulations. To disentangle the individual roles of sample size and geometry from thermal induced mobility, we compared simulations with obc and pbc, performed at low and room temperature. Our main finding is that small silica glass samples are ductile even at low temperatures and with pbc, suggesting that surface fluidization can not be the only cause for the experimentally observed behavior. We observed instead that departure from brittleness in small samples is due to the diffuse bond breaking before failure. This form of damage accumulation is found with both pbc and obc, at low and room temperatures.

A damage-dominated size-dependent transition similar to the one observed here was analyzed theoretically in an idealized network model for the fracture of quasi-brittle disordered solids.[27] According to the theory, a disordered network should always fail catastrophically in the infinite sample-size limit, unless the disorder is infinitely strong in which case bonds would fail one by one as in percolation. In the more relevant case of finite disorder in a finite sample, the theory predicts a finite-size critical regime characterized by a power-law distribution of stress drops and size-dependent scaling. In small samples, failure is dominated by the coalescence of many disorder-induced cracks, but as the sample size is increased, the probability to nucleate an unstable critical crack becomes larger. Hence, in large samples, the effect of disorder becomes less and less relevant, leading to brittle catastrophic failure.

The theoretical scenario discussed above is in agreement with the results of our simulations, showing power-law-distributed avalanches, size-dependent damage accumulation, and increased brittleness for larger sample sizes. The prediction of the theory do not specifically depend on the presence of a surface, in agreement with our results. Furthermore, the relevance of damage nucleation and accumulation in the failure of silica glass would be supported by in situ atomic force microscopy experiments in macroscopic samples, some of which describe the fracture propagation through the formation of nanoscale cavities ahead of the main crack.[31,32] This picture

DOI: 10.1021/acs.nanolett.8b00469
Nano Lett. 2018, 18, 4100−4106

was, however, questioned by other observations suggesting instead conventional brittle fracture.[33−35] Regardless of the exact mechanism of fracture propagation in macroscopic samples, our results show that coalescence of accumulated damage is the triggering mechanism of fracture in nanoscale samples.

Thermal effects provide an additional layer of complexity to the landscape, increasing surface mobility and inducing sample necking, in agreement with previous work.[9,10] Yet, the driver of the transition lies in the competition between disorder-induced diffuse damage and stress enhancement at the tip of the cracks. Statistically, larger samples will have longer cracks and therefore higher stresses at their tips, resulting in unstable crack propagation typical of brittle fracture.

Methods. *Obc Sample Preparation.* We have considered a set of seven cylindric samples, with the length, L, ranging from 10 to 80 nm and diameter, D, from 2.5 to 20 nm and with a fixed aspect ratio, $L/D = 4$ (see Table 1). For each size, N_{runs} statistically equivalent samples have been prepared starting from Si and O atoms randomly arranged in a cylindrical box. The number of atoms was chosen to match the target density, and the charge neutrality was maintained. Constraining the atoms to stay in a cylindrical configuration, a NVT quenching scheme from 4000 K down to 1 K was performed to anneal the silica liquid into a glassy state, with a nominal cooling rate of 50 K/ps. A time step of 1 fs was used. Afterward, an equilibration run was performed at $T = 1$ K for 20 ps upon the removal of the cylindrical constraint.

Table 1. Cylindrical Samples[a]

samples	L (nm)	D (nm)	N_{at}	N_{runs}
a	10	2.5	3282	100
b	15	3.7	11 076	100
c	20	5.0	26 250	100
d	30	7.5	87 900	100
e	40	10	210 000	100
f	60	15	708 000	74
g	80	20	1 680 000	15

[a]Size of the simulated cylindric silica glass nanofibers in terms of length, L, diameter, D, and total number of atoms, N_{at}. For each sample, the number, N_{runs}, of statistical realizations is also reported.

Pbc Sample Preparation. Periodic samples have been obtained starting from an orthogonal box of size $M \times M \times L$, with a square cross-sectional area matching that of the corresponding cylindrical sample, and periodic boundaries along all directions. After the same annealing procedure of the obc case, we have removed the pbc along z and performed an additional NPT relaxation step with cell relaxation along x-y in order to minimize the lateral pressure. The same lateral barostat was applied during the tensile deformation, using the same protocol described above.

Strain. The uniaxial tensile deformation was performed at a constant strain rate of $\lambda = 2.5 \times 10^8$ s^{-1}, by moving the external 5 Å of the sample (end-caps) with a constant velocity, $v = \lambda L/2$, along the axial z direction, right after an initial linear velocity ramp (10 ps) with $v = at$, where t is the simulation time and $a = 10^{-4}$ Å/fs^2. The end-caps atoms were free to move along the perpendicular x-y directions. Temperature and pressure were controlled by the Nosé−Hoover thermostat and barostat as implemented in LAMMPS,[36] with applied damping time factors of 1 and 10 ps, respectively.

Force Fields. Atomic interactions were described by the Watanabe potential,[37,38] an extension of the Stillinger−Weber (SW) potential,[39] which has been proven to well reproduce the experimental features of Si−O mixed systems also under an applied strain.[37,38,40,41] The force field consists of two terms: a two-body interaction that depends on distance and a three-body interaction that describes rotational and translational symmetry. The short cutoff distances and the replacement of the usual Coulomb interaction term by a coordination-based bond softening function for Si−O atoms accounting for the environmental dependence allow us to perform computationally efficient simulations of large-scale systems.

The density obtained with the Watanabe potential in a bulk system was $\rho_0 = 2.196$ g/cm^3, well matching the experimental value of 2.2 g/cm^3.[42] The effective radius, R, of the cylindric samples, which defines the volume, V, and thus the calculated stress, σ, was chosen at 50% of the normalized radial density profile. The radial density profile of all of the cylindric samples shows a smooth drop of the density at the fiber surface, with a skin size of about 0.5 nm (see Supporting Information, Figure S4). The surface roughness has been measured by considering the N_{surf} of most external atoms, with $N_{surf} = 2\pi RL\rho$, ρ being the surface density fixed to 10 atoms/nm^2. Given R_{avg}, the average radial position, from the cylinder axis, of these N_{surf} atoms, the surface roughness is calculated as a standard deviation of the radial coordinate from such average: $\sigma_s^2 = \langle (r - R_{avg})^2 \rangle$. The value σ_s is averaged over 20 randomly generated samples. For the $D = 2.5$ nm and $D = 5$ nm sizes, the average $\langle \sigma_s \rangle$ results 0.93 ± 0.15 Å and 0.90 ± 0.05 Å, respectively, showing no substantial variation of the surface roughness with the nanofiber size.

■ ASSOCIATED CONTENT

Supporting Information

The Supporting Information is available free of charge on the ACS Publications website at DOI: 10.1021/acs.nanolett.8b00469.

Size-dependent elastic modulus, mean square displacement, time-resolved displacement, radial density prole of the cylindric systems at 1 K, coordination, stress, kinetic and potential energy, variation of the Si−O−Si angle distribution during tensile deformation, total energy vs strength, stress-drops distribution and threshold, and waiting-time distributions between subsequent stress-drops (PDF)

Movie S1 (MPG)

Movie S2 (MPG)

Movie S3 (MPG)

Movie S4 (MPG)

■ AUTHOR INFORMATION

Corresponding Authors

*E-mail: ferrero@cab.cnea.gov.ar.

*E-mail: stefano.zapperi@unimi.it.

ORCID

Ezequiel E. Ferrero: 0000-0001-8516-6146

Roberto Guerra: 0000-0002-1278-8021

Stefano Zapperi: 0000-0001-5692-5465

Author Contributions

§S.B. and E.E.F. contributed equally to this work. S.Z. designed and coordinated the research. S.B., A.L.S., and R.G. performed

DOI: 10.1021/acs.nanolett.8b00469
Nano Lett. 2018, 18, 4100−4106

the simulations. S.B., E.E.F., and R.G., performed data analysis and produced figures and movies. S.B., E.E.F., R.G., and S.Z. wrote the manuscript.

Notes

The authors declare no competing financial interest.

■ ACKNOWLEDGMENTS

This research has been supported by ERC Advanced grant no. 291002 SIZEFFECTS. We thank J. L. Barrat, L. Cipelletti and A. Taloni for useful discussions.

■ REFERENCES

(1) Alava, M. J.; Nukala, P. K. V. V.; Zapperi, S. Statistical models of fracture. *Adv. Phys.* **2006**, *55*, 349−476.
(2) Lu, J.; Ravichandran, G.; Johnson, W. L. Deformation behavior of the Zr 41.2 Ti 13.8 Cu 12.5 Ni 10 Be 22.5 bulk metallic glass over a wide range of strain-rates and temperatures. *Acta Mater.* **2003**, *51*, 3429−3443.
(3) Yue, Y.; Zheng, K. Strong strain rate effect on the plasticity of amorphous silica nanowires. *Appl. Phys. Lett.* **2014**, *104*, 231906.
(4) Schuh, C. A.; Hufnagel, T. C.; Ramamurty, U. Mechanical behavior of amorphous alloys. *Acta Mater.* **2007**, *55*, 4067−4109.
(5) Li, G.; Jiang, M.; Jiang, F.; He, L.; Sun, J. Temperature-induced ductile-to-brittle transition of bulk metallic glasses. *Appl. Phys. Lett.* **2013**, *102*, 171901.
(6) Yuan, F.; Huang, L. Brittle to ductile transition in densified silica glass. *Sci. Rep.* **2015**, *4*, 1.
(7) Jang, D.; Greer, J. R. Transition from a strong-yet-brittle to a stronger-and-ductile state by size reduction of metallic glasses. *Nat. Mater.* **2010**, *9*, 215−219.
(8) Chen, D. Z.; Jang, D.; Guan, K. M.; An, Q.; Goddard, W. A.; Greer, J. R. Nanometallic Glasses: Size Reduction Brings Ductility, Surface State Drives Its Extent. *Nano Lett.* **2013**, *13*, 4462−4468.
(9) Luo, J.; Wang, J.; Bitzek, E.; Huang, J. Y.; Zheng, H.; Tong, L.; Yang, Q.; Li, J.; Mao, S. X. Size-Dependent Brittle-to-Ductile Transition in Silica Glass Nanofibers. *Nano Lett.* **2016**, *16*, 105−113.
(10) Wingert, M. C.; Kwon, S.; Cai, S.; Chen, R. Fluid-like Surface Layer and Its Flow Characteristics in Glassy Nanotubes. *Nano Lett.* **2016**, *16*, 7545−7550.
(11) Şopu, D.; Foroughi, A.; Stoica, M.; Eckert, J. Brittle-to-Ductile Transition in Metallic Glass Nanowires. *Nano Lett.* **2016**, *16*, 4467−4471.
(12) Hasan, M.; Kumar, G. High-throughput drawing and testing of metallic glass nanostructures. *Nanoscale* **2017**, *9*, 3261−3268.
(13) Chen, Y.-C.; Lu, Z.; Nomura, K.-i.; Wang, W.; Kalia, R. K.; Nakano, A.; Vashishta, P. Interaction of Voids and Nanoductility in Silica Glass. *Phys. Rev. Lett.* **2007**, *99*, 155506.
(14) Pradeep, N.; Kim, D.-I.; Grobelny, J.; Hawa, T.; Henz, B.; Zachariah, M. R. Ductility at the nanoscale: Deformation and fracture of adhesive contacts using atomic force microscopy. *Appl. Phys. Lett.* **2007**, *91*, 203114.
(15) Tang, C.; Dávila, L. P. Anomalous surface states modify the size-dependent mechanical properties and fracture of silica nanowires. *Nanotechnology* **2014**, *25*, 435702.
(16) Tang, C.; Dávila, L. P. Strain-induced structural modifications and size-effects in silica nanowires. *J. Appl. Phys.* **2015**, *118*, 094302.
(17) Kim, Y.-J.; Lee, W. W.; Choi, I.-C.; Yoo, B.-G.; Han, S. M.; Park, H.-G.; Park, W. I.; Jang, J.-i. Time-dependent nanoscale plasticity of ZnO nanorods. *Acta Mater.* **2013**, *61*, 7180−7188.
(18) Cheng, G.; Miao, C.; Qin, Q.; Li, J.; Xu, F.; Haftbaradaran, H.; Dickey, E. C.; Gao, H.; Zhu, Y. Large anelasticity and associated energy dissipation in single-crystalline nanowires. *Nat. Nanotechnol.* **2015**, *10*, 687−691.
(19) Fakhraai, Z.; Forrest, J. Measuring the surface dynamics of glassy polymers. *Science* **2008**, *319*, 600−604.
(20) Chai, Y.; Salez, T.; McGraw, J. D.; Benzaquen, M.; Dalnoki-Veress, K.; Raphaël, E.; Forrest, J. A. A direct quantitative measure of surface mobility in a glassy polymer. *Science* **2014**, *343*, 994−999.
(21) Coslovich, D.; Pastore, G. Dynamics and energy landscape in a tetrahedral network glass-former: direct comparison with models of fragile liquids. *J. Phys.: Condens. Matter* **2009**, *21*, 285107.
(22) Horbach, J.; Kob, W.; Binder, K.; Angell, C. A. Finite size effects in simulations of glass dynamics. *Phys. Rev. E: Stat. Phys., Plasmas, Fluids, Relat. Interdiscip. Top.* **1996**, *54*, R5897.
(23) Harkless, J. A. W.; Stillinger, D. K.; Stillinger, F. H. Structures and Energies of SiO_2 Clusters. *J. Phys. Chem.* **1996**, *100*, 1098−1103.
(24) Laurson, L.; Illa, X.; Santucci, S.; Tallakstad, K. T.; Maloy, K. J.; Alava, M. J. Evolution of the average avalanche shape with the universality class. *Nat. Commun.* **2013**, *4*, 1.
(25) Liu, C.; Ferrero, E. E.; Puosi, F.; Barrat, J.-L.; Martens, K. Driving Rate Dependence of Avalanche Statistics and Shapes at the Yielding Transition. *Phys. Rev. Lett.* **2016**, *116*, 065501.
(26) Janićević, S.; Laurson, L.; Måløy, K. J.; Santucci, S.; Alava, M. J. Interevent Correlations from Avalanches Hiding Below the Detection Threshold. *Phys. Rev. Lett.* **2016**, *117*, 230601.
(27) Shekhawat, A.; Zapperi, S.; Sethna, J. P. From Damage Percolation to Crack Nucleation Through Finite Size Criticality. *Phys. Rev. Lett.* **2013**, *110*, 185505.
(28) Nicolas, A.; Ferrero, E. E.; Martens, K.; Barrat, J.-L. Deformation and flow of amorphous solids: a review of mesoscale elastoplastic models. **2017**, arXiv preprint arXiv:1708.09194.
(29) Bouzid, M.; Colombo, J.; Barbosa, L. V.; Del Gado, E. Elastically driven intermittent microscopic dynamics in soft solids. *Nat. Commun.* **2017**, *8*, 15846.
(30) Pedone, A.; Malavasi, G.; Menziani, M. C.; Segre, U.; Cormack, A. N. Molecular dynamics studies of stress- strain behavior of silica glass under a tensile load. *Chem. Mater.* **2008**, *20*, 4356−4366.
(31) Célarié, F.; Prades, S.; Bonamy, D.; Ferrero, L.; Bouchaud, E.; Guillot, C.; Marlière, C. Glass Breaks like Metal, but at the Nanometer Scale. *Phys. Rev. Lett.* **2003**, *90*, 075504.
(32) Bonamy, D.; Prades, S.; Rountree, C. L.; Ponson, L.; Dalmas, D.; Bouchaud, E.; Ravi-Chandar, K.; Guillot, C. Nanoscale damage during fracture in silica glass. *Int. J. Fract.* **2006**, *140*, 3−14.
(33) Guin, J. P.; Wiederhorn, S. M. Fracture of silicate glasses: Ductile or brittle? *Phys. Rev. Lett.* **2004**, *92*, 215502.
(34) López-Cepero, J. M.; Wiederhorn, S. M.; Fett, T.; Guin, J. P. Do plastic zones form at crack tips in silicate glasses? *Int. J. Mater. Res.* **2007**, *98*, 1170−1176.
(35) Fett, T.; Rizzi, G.; Creek, D.; Wagner, S.; Guin, J. P.; López-Cepero, J. M.; Wiederhorn, S. M. Finite element analysis of a crack tip in silicate glass: No evidence for a plastic zone. *Phys. Rev. B: Condens. Matter Mater. Phys.* **2008**, *77*, 174110.
(36) Plimpton, S. Fast parallel algorithms for short-range molecular dynamics. *J. Comput. Phys.* **1995**, *117*, 1−19.
(37) Watanabe, T.; Fujiwara, H.; Noguchi, H.; Hoshino, T.; Ohdomari, I. Novel interatomic potential energy function for Si, O mixed systems. *Japanese journal of applied physics* **1999**, *38*, L366.
(38) Watanabe, T.; Yamasaki, D.; Tatsumura, K.; Ohdomari, I. Improved interatomic potential for stressed Si, O mixed systems. *Appl. Surf. Sci.* **2004**, *234*, 207−213.
(39) Stillinger, F. H.; Weber, T. A. Computer simulation of local order in condensed phases of silicon. *Phys. Rev. B: Condens. Matter Mater. Phys.* **1985**, *31*, 5262.
(40) Dalla Torre, J.; Bocquet, J.-L.; Limoge, Y.; Crocombette, J.-P.; Adam, E.; Martin, G.; Baron, T.; Rivallin, P.; Mur, P. Study of self-limiting oxidation of silicon nanoclusters by atomistic simulations. *J. Appl. Phys.* **2002**, *92*, 1084−1094.
(41) Djurabekova, F.; Nordlund, K. Atomistic simulation of the interface structure of Si nanocrystals embedded in amorphous silica. *Phys. Rev. B: Condens. Matter Mater. Phys.* **2008**, *77*, 115325.
(42) Brückner, R. Properties and structure of vitreous silica. II. *J. Non-Cryst. Solids* **1971**, *5*, 177−216.

DOI: 10.1021/acs.nanolett.8b00469
Nano Lett. 2018, 18, 4100−4106